

Resilience of the Iron Environment in Heme Proteins

Bogdan M. Leu,^{*,‡} Yong Zhang,[†] Lintao Bu,[†] John E. Straub,[†] Jiyong Zhao,[‡] Wolfgang Sturhahn,[‡] E. Ercan Alp,[‡] and J. Timothy Sage^{*}

^{*}Department of Physics and Center for Interdisciplinary Research on Complex Systems, Northeastern University, Boston, Massachusetts;

[†]Department of Chemistry, Boston University, Boston, Massachusetts; and [‡]Advanced Photon Source, Argonne National Laboratory, Argonne, Illinois

ABSTRACT Conformational flexibility is essential to the functional behavior of proteins. We use an effective force constant introduced by Zaccai, the resilience, to quantify this flexibility. Site-selective experimental and computational methods allow us to determine the resilience of heme protein active sites. The vibrational density of states of the heme Fe determined using nuclear resonance vibrational spectroscopy provides a direct experimental measure of the resilience of the Fe environment, which we compare quantitatively with values derived from the temperature dependence of atomic mean-squared displacements in molecular dynamics simulations. Vibrational normal modes in the THz frequency range dominate the resilience. Both experimental and computational methods find a higher resilience for cytochrome *c* than for myoglobin, which we attribute to the increased number of covalent links to the peptide in the former protein. For myoglobin, the resilience of the iron environment is larger than the average resilience previously determined for hydrogen sites using neutron scattering. Experimental results suggest a slightly reduced resilience for cytochrome *c* upon oxidation, although the change is smaller than reported in previous Mössbauer investigations on a bacterial cytochrome *c*, and is not reproduced by the simulations. Oxidation state also has no significant influence on the compressibility calculated for cyt *c*, although a slightly larger compressibility is predicted for myoglobin.

INTRODUCTION

Many biological functions of biomolecules rely on their dynamical characteristics (1). Quantitative measurements of atomic mean-squared displacements (MSD) provide an important experimental probe of dynamics. Temperature-dependent MSD measurements on proteins reveal a nearly linear dependence at low temperatures, followed by an abrupt increase above 200 K (1–6). The linear dependence is consistent with quasiharmonic vibrational motions about local minima on the energy surface, while thermally activated transitions among these minima are proposed to account for the abrupt increase above 200 K. Some protein reactions, such as geminate CO rebinding to myoglobin (Mb) (7) and electrostatic relaxation in the green fluorescent protein (8), can proceed below 200 K. However, processes such as CO escape from the interior of Mb (7) and some (9), but not all (10), enzymatic reactions apparently require the activation of protein-specific dynamics above the 200 K dynamical transition. Dehydration suppresses the transition, and simulations and correlation with solvent dielectric properties suggests that the protein dynamics are coupled with solvent fluctuations (11,12).

Although some aspects of protein dynamical behavior are likely to be generic, comparison of different proteins might reveal dynamical variations relevant to differences in functional behavior. In fact, reactivity may depend crucially upon local dynamical and mechanical properties of a protein active

site (13). The means by which the static structure influences local reactivity are heavily investigated, but the structural dynamics are likely to be equally crucial.

Two simple heme proteins that have served as models for the interplay of protein structure, function, and dynamics are Mb, which stores and transports oxygen by reversibly binding and releasing molecular oxygen from the heme Fe (14), and cytochrome *c* (cyt *c*), which facilitates an essential step in oxidative phosphorylation by transporting electrons to cyt *c* oxidase (15) (Fig. 1). While each heme is covalently linked to the protein backbone through a bond between the heme Fe and the imidazole N_ε of a histidine side chain, cyt *c* has three additional links to the protein. Methionine sulfur forms a second bond to the heme Fe, and two cysteine residues form thioether links to the vinyl groups at the periphery of the heme group. It is likely that these structural differences influence both the reactivity and the mechanical properties of the heme environment.

The effect of the oxidation state of the Fe on protein structure, dynamics, and reactivity has been heavily investigated for cyt *c*. Although structural differences between oxidized and reduced cyt *c* are small, both in the crystal (16,17) and in solution (18,19), the native state of the oxidized protein is less stable. The oxidation state influences hydrodynamic, thermodynamic, and spectroscopic properties, as well as ion binding and chemical reactivity ((20) and references therein). The Fe-S(Met-80) bond is shorter in the reduced form (21) and less easily displaced by exogenous ligands (20).

Recent measurements yield varying results regarding the influence of oxidation state on the vibrational dynamics of cyt

Submitted May 28, 2008, and accepted for publication July 22, 2008.

Address reprint requests to J. Timothy Sage, Tel.: 617-373-2908; E-mail: jtsage@neu.edu.

Editor: Betty J. Gaffney.

© 2008 by the Biophysical Society
0006-3495/08/12/5874/16 \$2.00

doi: 10.1529/biophysj.108.138198

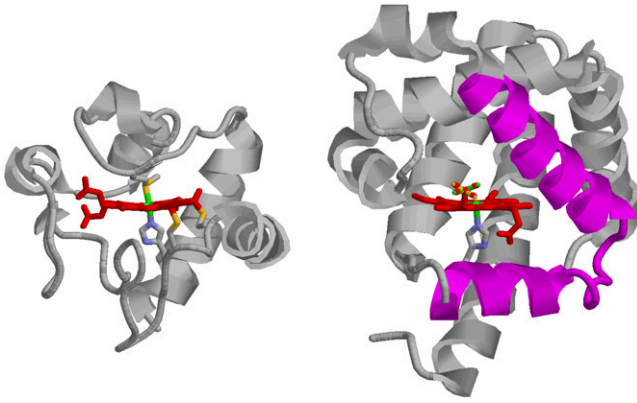


FIGURE 1 Structural comparison of *cyt c* (left) with deoxyMb (right). In both proteins, a histidine (His-18 in *cyt c* and His-93 in Mb) binds to the heme Fe. In *cyt c*, a bond from Met-80 to the Fe and thioether bridges from Cys-14 and Cys-17 to the vinyl groups forms additional covalent links between heme and polypeptide. Structural depictions are based on coordinates deposited in the Protein Data Bank with access codes 1HRC (63) and 1BZR (67).

c. Mössbauer measurements on a bacterial *cyt c* suggest an increased Fe MSD upon oxidation (22), and THz measurements reveal increased absorption in the oxidized state (23). On the other hand, methyl C-D vibrations of the Met-80 ligand provide no indication that Fe oxidation affects the vibrational dynamics of the active site (24).

Here, we report experiments and simulations that explore the influence of protein structure on the dynamics of the heme Fe for reduced and oxidized *cyt c* and for deoxygenated Mb (deoxyMb). The Fe-weighted vibrational density of states (VDOS) derived from nuclear resonance vibrational spectroscopy (NRVS) (25,26) quantitatively predicts a temperature-dependent vibrational contribution to the Fe MSD. Molecular dynamics (MD) simulations track the vibrational MSD below 200 K. Together, these results provide direct evidence that vibrational motion dominates the dynamics of the Fe at low temperature, and suggest activation of additional motions on longer timescales above 200 K. Moreover, frequencies below 100 cm^{-1} dominate the vibrational MSD of the Fe, with a prominent contribution from translational motion of the heme core.

The limiting slope of the vibrational MSD determines an effective force constant, the resilience (6), which facilitates comparison among the different methods and different proteins. Both simulations and experiments reported here reveal a higher resilience for the Fe environment in *cyt c* than in Mb, which we attribute to the additional covalent bonds between the heme and the protein, and also indicate a higher resilience for the Fe environment than the average resilience of hydrogen sites, previously determined from neutron scattering measurements on Mb (6,27). Although our experimental results indicate a slight reduction in the resilience of *cyt c* in the oxidized state, it is significantly smaller than that suggested by Mössbauer measurements on a bacterial *cyt c* (22), and is not reproduced in the simulations. Similarly, the Fe

VDOS of oxidized and reduced *cyt c* are indistinguishable in the 20–100 cm^{-1} frequency region, although both are significantly reduced in comparison with deoxyMb.

ATOMIC FLUCTUATIONS AND MOLECULAR RESILIENCE

Chemical and biological reactions depend on the motions of the constituent atoms. At short times or low temperatures, this motion consists of oscillations about well-defined equilibrium positions, with amplitudes that fluctuate because of interactions with a thermal bath. Occasionally, the magnitude of these thermal fluctuations is sufficient to carry the system across an energy barrier to a new local minimum on the energy surface. The timescales for the latter activated processes depend strongly both on the temperature and on the shape of the energy surface.

Measurements of the MSD $\langle x_j^2 \rangle$ of atom j from its equilibrium position provide an experimental means of characterizing atomic motion on this energy surface. The signal observed in many experiments results from averaging a phase factor $e^{i\vec{k}\cdot\vec{r}_j}$ over a distribution of atomic displacements \vec{r}_j from their equilibrium positions. When these displacements are assumed to have a Gaussian distribution, the experimental signal is proportional to a factor

$$f = |\langle e^{i\vec{k}\cdot\vec{r}_j} \rangle_\tau|^2 = \exp[-k^2 \langle x_j^2 \rangle_\tau], \quad (1)$$

that depends exponentially on the MSD.

The angle brackets $\langle \dots \rangle_\tau$ represent an average over an ensemble of molecules, while the subscript acknowledges the additional implicit averaging of the MSD over a finite timescale τ that takes place in many measurements and in calculations. Computationally, this timescale is determined by the finite length of a simulation. Experimentally, the energy resolution determines τ through the uncertainty principle. This Gaussian approximation holds for a variety of simple cases such as simple Brownian diffusion or harmonic vibrations.

The MSD-dependent factor in Eq. 1 is often viewed as an experimental limitation. X-ray crystallographers know it as the Debye-Waller factor (28), which reduces the measured intensity at large values of the scattering vector \vec{k} and thus limits achievable spatial resolution (29). Mössbauer spectroscopists recognize it as the Lamb-Mössbauer factor or recoilless fraction, which determines the spectral area. Increasing motion of the Mössbauer nucleus at high temperatures eventually reduces the Mössbauer signal to unobservable levels (30–33).

On the other hand, Eq. 1 supplements static information about atomic (equilibrium) positions with dynamical information about atomic fluctuations. This dynamical information can be obtained more directly by measuring inelastic scattering of neutrons (34,35) or x-rays (36,37) from solutions, which eliminates contributions from static lattice dis-

order so that the MSD is determined purely by dynamics. However, the dynamical information is averaged over all atoms that have significant scattering amplitudes.

Careful measurements of nuclear resonance absorption reveal dynamical information specific to a particular isotope. Conventional Mössbauer measurements yield a recoilless fraction that takes the form of Eq. 1 (32,33), where the resonance energy E_0 determines the magnitude $k = E_0/\hbar c$ of the wave vector of the absorbed photon, while NRVS measurements over a wider energy range reveal the complete spectrum of Fe vibrations that contribute to the MSD (25,26).

The MSD depends strongly on temperature, and Zaccai (6) has introduced the concept of a resilience

$$k_r = \frac{k_B}{d\langle x_j^2 \rangle / dT}, \quad (2)$$

having dimensions of a force constant, to describe the temperature dependence of atomic fluctuations. The resilience provides a compact description of atomic fluctuations when the temperature variation of the MSD is nearly linear. Examples of situations where this occurs are when the MSD is dominated by harmonic fluctuations in the classical (high temperature) limit or by classical diffusion in the presence of temperature-independent friction. Zaccai has described the well-known transition in the dynamical behavior of proteins near 200 K (3,5,38) as a decrease (by approximately an order of magnitude for myoglobin) in the resilience of the protein atoms as they transform from quasiharmonic vibrations around potential minima at low temperatures to quasidiffusive hopping among minima at high temperature (6).

To avoid possible confusion, we note that the resilience as defined by Eq. 1 is a factor of 3 larger than that given by Zaccai (6), corresponding to an average (rather than a sum) over the direction of motion. We further emphasize that this concept has no direct relation to the modulus of resilience defined in engineering practice as an integral of the elastic region of the stress-strain curve (39).

The following section demonstrates that the resilience of a probe atom j takes a particularly simple form for a harmonic system, determined by the VDOS. NRVS measurements at a single temperature yield the VDOS for ^{57}Fe , and therefore the resilience of the Fe environment. In contrast, previous determinations of the resilience (6,35) required systematic measurements of the MSD at a series of temperatures and represent an average over many molecular sites.

HARMONIC APPROXIMATION

Introduction of the harmonic approximation enables straightforward extrapolation of the vibrational properties determined at a single temperature to determine the MSD as a function of temperature. In general, linear transformation coefficients $\vec{e}_{j\alpha}$ relate the Cartesian displacement

$$\vec{r}_j = \sum_{\alpha} \vec{e}_{j\alpha} Q_{\alpha} / m_j^{1/2} \quad (3)$$

of atom j , with mass m_j , from its equilibrium position to a set of mass weighted normal coordinates Q_{α} (26). In the harmonic approximation, variations of the molecular energy higher than quadratic in the atomic displacements are neglected, and the normal coordinates are chosen to eliminate cross terms from the nuclear Hamiltonian

$$\mathcal{H} = \sum_{\alpha} \left[-\frac{1}{2} \hbar^2 \frac{\partial^2}{\partial Q_{\alpha}^2} + \frac{1}{2} \omega_{\alpha}^2 Q_{\alpha}^2 \right], \quad (4)$$

that governs the motion of the atomic centers of mass.

Vibrational excitation numbers n_{α} specify the eigenstates as direct products

$$|\{n\}\rangle = |n_1\rangle \otimes |n_2\rangle \otimes |n_3\rangle \otimes |n_4\rangle \otimes \dots \quad (5)$$

of eigenstates for individual oscillators, which have the well-known properties of the one-dimensional quantum harmonic oscillator (40,41). We follow a common spectroscopic convention by expressing the angular frequency $\omega_{\alpha} = 2\pi c \bar{\nu}_{\alpha}$ of a normal mode in terms of the inverse free space wavelength $\bar{\nu}_{\alpha}$ of a photon with the corresponding energy.

The vibrational contribution to the thermally averaged MSD

$$\langle x_j^2 \rangle_v = \langle (\hat{k} \cdot \vec{r}_j)^2 \rangle_v = \frac{1}{m_j} \sum_{\alpha\beta} (\hat{k} \cdot \vec{e}_{j\alpha}) (\hat{k} \cdot \vec{e}_{j\beta}) \langle Q_{\alpha} Q_{\beta} \rangle_T \quad (6)$$

of atom j along the beam direction \hat{k} depends on the thermally averaged expectation values

$$\langle Q_{\alpha} Q_{\beta} \rangle_T = \sum_{\{n_{\alpha}\}} p(\{n\}) \langle \{n\} | Q_{\alpha} Q_{\beta} | \{n\} \rangle \quad (7)$$

of products of normal coordinate operators, weighted by the probability

$$p(\{n\}) = \prod_{\alpha} \left[\frac{\exp(-n_{\alpha} \hbar c \bar{\nu}_{\alpha} / k_B T)}{\sum_{n_{\alpha}} \exp(-n_{\alpha} \hbar c \bar{\nu}_{\alpha} / k_B T)} \right]$$

of each vibrational state at temperature T . The matrix element

$$\langle \{n\} | Q_{\alpha} Q_{\beta} | \{n\} \rangle = (2n_{\alpha} + 1) \frac{\hbar}{2\omega_{\alpha}} \delta_{\alpha\beta} \quad (8)$$

is easily evaluated using the properties

$$\langle n_{\alpha} | Q_{\alpha} | n_{\alpha} \rangle = 0 \quad (9)$$

and

$$\langle n_{\alpha} | Q_{\alpha}^2 | n_{\alpha} \rangle = \frac{\hbar}{2\omega_{\alpha}} (2n_{\alpha} + 1) \quad (10)$$

of a one-dimensional quantum harmonic oscillator (40,41). The temperature dependence of the resulting expression

$$\langle x_j^2 \rangle_v = \frac{1}{k^2} \sum_{\alpha} (\hat{k} \cdot \vec{e}_{j\alpha})^2 [2n(\bar{\nu}_{\alpha}) + 1] \frac{\bar{\nu}_R}{\bar{\nu}_{\alpha}} \quad (11)$$

for the atomic MSD of atom j resulting from substitution into Eq. 6 results only from the thermally averaged occupation factor

$$n(\bar{\nu}_{\alpha}) = [\exp(hc\bar{\nu}_{\alpha}/k_B T) - 1]^{-1} \quad (12)$$

of a mode with frequency $\bar{\nu}_{\alpha}$. In anticipation of the experimental approach to be used in this article, Eq. 11 introduces the recoil energy $hc\bar{\nu}_R = \hbar^2 k^2 / 2m_j$ of a free nucleus of mass m_j absorbing a photon of energy $E = \hbar ck$. For the ^{57}Fe NRVS measurements reported below, $\bar{\nu}_R = 15.8 \text{ cm}^{-1}$ because the photon energy $\hbar ck$ scans over a very small range within 100 meV of the nuclear excitation energy $E_0 = 14.4 \text{ keV}$.

A more compact description of the MSD in terms of the VDOS

$$D_k(\bar{\nu}) = \sum_{\alpha} (\hat{k} \cdot \vec{e}_{j\alpha})^2 \mathcal{L}(\bar{\nu} - \bar{\nu}_{\alpha}) \quad (13)$$

projected along the direction \hat{k} of the beam is justified as long as the widths of the lineshape functions (normalized as $\int \mathcal{L}(\bar{\nu} - \bar{\nu}_{\alpha}) d\bar{\nu} = 1$) can be neglected relative to the mode frequency (26). For randomly oriented molecules, as typical for a solution, orientational averaging yields $\langle (\hat{k} \cdot \vec{e}_{j\alpha})^2 \rangle = \frac{1}{3} e_{j\alpha}^2$, and the MSD

$$\langle x_j^2 \rangle_v = \frac{1}{3k^2} \int_0^{\infty} [2\bar{n}(\bar{\nu}) + 1] \frac{\bar{\nu}_R}{\bar{\nu}} D(\bar{\nu}) d\bar{\nu} \quad (14)$$

depends on the total VDOS

$$D(\bar{\nu}) = \sum_{\alpha} e_{j\alpha}^2 \mathcal{L}(\bar{\nu} - \bar{\nu}_{\alpha}) \quad (15)$$

for atom j . The factor of 3 reflects the normalization $\int D(\bar{\nu}) d\bar{\nu} = \sum_{\alpha} e_{j\alpha}^2 = 3$ of the VDOS (26).

The temperature dependence of the MSD determines the vibrational contribution to the resilience, which has a well-defined limiting value at sufficiently high temperatures to justify the approximation $k_B T \gg hc\bar{\nu}$. In this limit, the thermal factor

$$2n(\bar{\nu}) + 1 = \frac{2k_B T}{hc\bar{\nu}} \quad (16)$$

and thus the MSD

$$\langle x_j^2 \rangle = k_B T \frac{2\bar{\nu}_R}{\hbar c k^2} \frac{1}{3} \int_0^{\infty} \frac{D(\bar{\nu})}{\bar{\nu}^2} d\bar{\nu} \quad (17)$$

depend linearly on temperature, and the resilience

$$k_r = m_j \langle \omega^{-2} \rangle^{-1} \quad (18)$$

determined by the definition in Eq. 2 depends on the inverse mean-square frequency

$$\langle \omega^{-2} \rangle = \frac{1}{3} \int_0^{\infty} \frac{D(\omega)}{\omega^2} d\omega \quad (19)$$

averaged according to the VDOS for atom j .

The high temperature limit (Eq. 17) of the MSD extrapolates to $\langle x_j^2 \rangle_v = 0$ in the limit $T \rightarrow 0$. However, the general expression (Eq. 14) does not vanish, but instead approaches a finite value

$$\langle x_j^2 \rangle_0 = \frac{\bar{\nu}_R}{k^2} \frac{1}{3} \int_0^{\infty} \frac{D(\bar{\nu})}{\bar{\nu}} d\bar{\nu} \quad (20)$$

determined by zero-point motion of the oscillating atom. Comparison of these two limiting cases quantitatively identifies the temperature

$$T^* = \frac{hc}{2k_B} \frac{\int_0^{\infty} \bar{\nu}^{-1} D(\bar{\nu}) d\bar{\nu}}{\int_0^{\infty} \bar{\nu}^{-2} D(\bar{\nu}) d\bar{\nu}} \quad (21)$$

at which the extrapolated high temperature MSD (Eq. 17) first exceeds the zero-point contribution (Eq. 20). The high temperature approximation may reasonably be applied for temperatures $T \gg T^*$.

As an example, solid lines in Fig. 2 show the temperature-dependent MSD calculated from Eq. 14 using the experimentally determined VDOS for protein data presented in a later section. (*Markers* in Fig. 2 are independently determined using Eq. 24 below to confirm self-consistency of the procedure.) The VDOS for Fe(II) cyt *c*, Fe(III) cyt *c*, and deoxyMb yield turnover temperatures $T^* = 41, 38, \text{ and } 33 \text{ K}$, respectively, from Eq. 21. As a result, all three curves approach the limiting high temperature slope of Eq. 17, as indicated by the dashed line, above 100 K. At 300 K, deviations between Eqs. 14 and 17 are $< 2\%$.

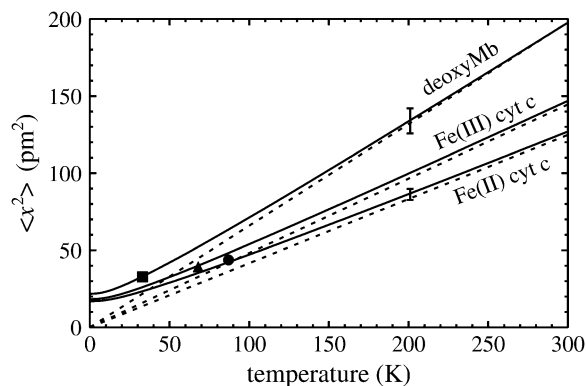


FIGURE 2 Temperature dependence of the vibrational contribution to the Fe MSD for Fe(II) and Fe(III) cyt *c* and for deoxyMb, extrapolated to the Fe VDOS $D(\bar{\nu})$ measured at a single temperature using Eq. 14. The error bars represent the uncertainty in determining the sample temperature and instrumental background (see the text for details). Dashed lines indicate the limiting high temperature slopes that determine the vibrational resilience through Eq. 2. The markers (*circle* for Fe(II) cyt *c*, *triangle* for Fe(III) cyt *c*, and *square* for deoxyMb, respectively) represent the Fe mean-square displacement at the experimental temperature, with the Lamb-Mössbauer factor f determined from the integrated area $(1-f)$ of $S'(\bar{\nu})$.

METHODS

^{57}Fe reconstitution

We prepared ^{57}Fe -reconstituted cyt *c* by extracting the iron from the heme and reconstituting the resulting porphyrin cyt *c* with ^{57}Fe . We have employed two different procedures to remove the iron from oxidized native cyt *c* at low pH (42). One, adapted from the experiments carried out by Vanderkooi and Erecinska (43), with minor modifications of the methods of Robinson and Kamen (44) and Fisher et al. (45), involves the use of hydrofluoric acid. For the results presented here, we followed an alternate procedure (46), which uses a solution of ferrous sulfate in hydrochloric acid. This method avoids the hazards of working with hydrofluoric acid and gives a spectroscopically identical product, but with a smaller yield (42).

Insertion of ^{57}Fe in the resulting porphyrin cyt *c* took place upon incubation with ^{57}Fe -enriched ferrous acetate in a pH 5 solution at 70°C under strictly anaerobic conditions. We synthesized ferrous acetate according to methods described by Warburg and Negelein (47), Flatmark and Robinson (48), Koch (49), and Hardt and Möller (50). The complete experimental procedure is described elsewhere (42).

Preparation of ^{57}Fe -enriched myoglobin has been described previously (51). Briefly, a milder procedure described by Teale (52) allows us to remove the entire heme, which is not covalently attached to the polypeptide backbone. The resulting apoprotein is reconstituted with oxidized ^{57}Fe -enriched heme (protoporphyrin IX) obtained from Frontier Scientific (Logan, UT).

Extensive centrifugation of solutions of reconstituted protein in micro-concentrators (Centricon, Houston, TX) led to final concentrations of 5, 8, and 13 mM for reduced cyt *c*, oxidized cyt *c*, and deoxymyoglobin, respectively. Oxidation of cyt *c* followed addition of a concentrated solution of potassium ferricyanide to the reduced protein solution resulting from reconstitution, while deoxyMb was prepared by adding one drop of a deoxygenated 1 M solution of sodium dithionite to the concentrated solution of ^{57}Fe -enriched myoglobin. Absorption measurements of the heme Soret band after quantitative dilution of the concentrated solutions determined the concentration and also verified the heme oxidation state.

NRVS measurements and analysis

NRVS measurements were performed at sector 3-ID-D of the Advanced Photon Source, and data collection and analysis are described in detail elsewhere (25,53). Briefly, sample cells containing concentrated protein solutions were maintained at low temperature in a helium flow cryostat. A polyethylene window on the sample cell and a beryllium dome on the cryostat provided access for a highly monochromatic incident x-ray beam that could be tuned through the 14.4 keV ^{57}Fe resonance and for collection of the resulting x-ray emission at 6.4 and 14.4 keV.

Data accumulation was disabled during a time interval containing the incident x-ray pulse, thus restricting detection to photons resulting from excitation of the nuclear resonance, which arrive with a delay on the order of the 141-ns nuclear excited-state lifetime. The resulting delayed signal was recorded as a function of the incident photon energy E . Enforcement of Lipkin's first moment sum rule (54,55) yielded a normalized excitation probability $S(\bar{\nu})$ as a function of the energy separation $hc\bar{\nu} = E - E_0$ from the recoilless resonance energy $E_0 = 14.4125$ keV. The vibrational contribution $S'(\bar{\nu})$ to the excitation probability results from weighted subtraction of an instrumental resolution function determined by recording the nuclear forward scattering of the beam from an ^{57}Fe foil, for which vibrational contributions are negligible.

We use the program PHOENIX (56) to find the VDOS $D(\bar{\nu})$ from the one-quantum contribution

$$S_1(\bar{\nu}) = \frac{1}{3} f \frac{\bar{\nu}_R}{\bar{\nu}} [\bar{n}(\bar{\nu}) + 1] D(\bar{\nu}) \quad (22)$$

to the total vibrational signal

$$S'(\bar{\nu}) = S_1(\bar{\nu}) + S_2(\bar{\nu}) + S_3(\bar{\nu}) + \dots \quad (23)$$

PHOENIX determines $S_1(\bar{\nu})$ by implementing the Fourier-log deconvolution algorithm (57), which is applicable to harmonic systems if vibrational anisotropy can be neglected in the calculation of higher order contributions ($S_n(\bar{\nu})$ with $n > 1$) from $S_1(\bar{\nu})$. The area of the vibrational excitation probability $S'(\bar{\nu})$ determines the recoilless fraction

$$f = 1 - \int_{-\infty}^{\infty} S'(\bar{\nu}) d\bar{\nu} \quad (24)$$

and thus the Fe MSD at the experimental temperature according to Eq. 1.

Analysis of experimental data (Fig. 3) indicates that higher order vibrational contributions are small enough that the assumptions involved in the log-normal procedure do not lead to significant uncertainty in determination of $D(\bar{\nu})$ for Fe(III) cyt *c*. Moreover, results on deoxyMb and Fe(II) cyt *c* follow expectations based on assuming a Debye frequency dependence

$$D(\bar{\nu}) = a\bar{\nu}^2 \quad (25)$$

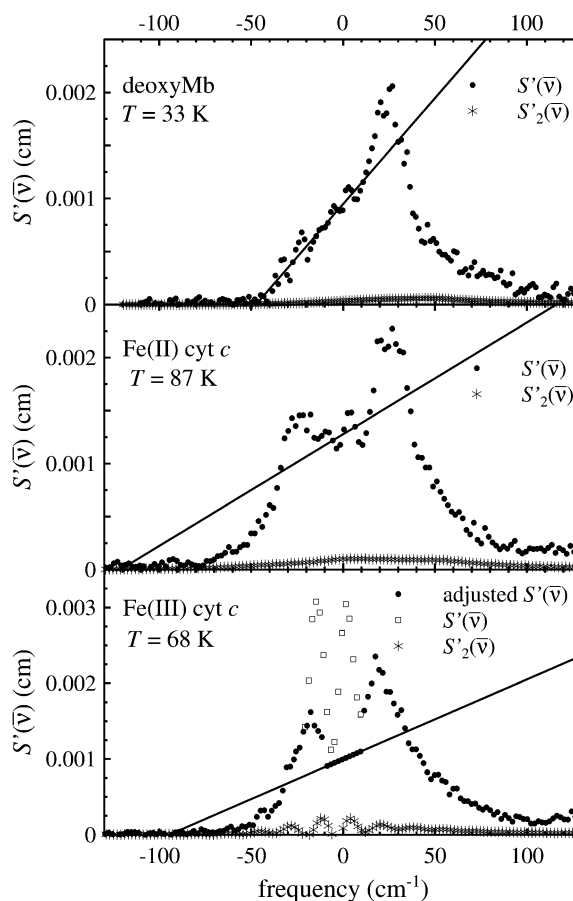


FIGURE 3 The vibrational component $S'(\bar{\nu})$ of the excitation probability determined for deoxyMb, Fe(II) cyt *c*, and Fe(III) cyt *c*. Peaks near 25 cm^{-1} reflect a slight excess above the Debye extrapolation from the $[-10, 10]$ cm^{-1} interval, as described in the text and indicated by the thin line. One-phonon excitations $S'_1(\bar{\nu})$ dominate the signal, while two-phonon contributions $S'_2(\bar{\nu})$ (asterisks) are much weaker, justifying the neglect of multiphonon contributions (Eq. 23). Fe(III) cyt *c* data compromised by imperfect subtraction of the resolution function are indicated by open squares and were replaced with points marked by solid circles according to the Debye extrapolation procedure described in the text.

at sufficiently low frequency. Substitution of Eq. 25 into Eq. 22 and low-energy expansion of the expression (Eq. 12) for the occupation number shows that the excitation probability

$$S'(\bar{\nu}) \simeq S_1(\bar{\nu}) = \frac{af\bar{\nu}_R}{6}(\bar{\nu} + \bar{\nu}_0) \quad (26)$$

depends linearly on frequency for sufficiently low frequencies, with the extrapolated intercept $-\bar{\nu}_0$ with the negative frequency axis determined by the sample temperature

$$T = \frac{hc\bar{\nu}_0}{2k_B}. \quad (27)$$

Lines in Fig. 3 follow Eq. 26, with intercepts determined by the experimental temperature according to Eq. 27. A least-squares fit to data in the $[-10, 10] \text{ cm}^{-1}$ interval determined the slopes for deoxyMb and Fe(II) cyt *c*. Comparison with the experimental data shown in the upper panels of Fig. 3 suggest, in agreement with previous work (58), that Eq. 25 is a reasonable approximation for proteins in this interval. At higher frequencies, density in excess of the Debye extrapolation appears with a peak near 30 cm^{-1} . The similarity to the Boson peak observed in glasses has been noted (58).

However, it is evident from the lower panel of Fig. 3 that imperfect subtraction of the recoilless line complicates determination of the vibrational contributions below 20 cm^{-1} for Fe(III) cyt *c*. To analyze these results, we approximate the low frequency region by assuming that the excitation probability follows the linear Debye extrapolation expressed in Eq. 26. We further assume that the slope of the extrapolation is the same as that determined experimentally for Fe(II) cyt *c*, and use the 68 K experimental temperature to fix the intercept $\bar{\nu}_0$ according to Eq. 27. We then replace points in the $[-8.6, 9.5] \text{ cm}^{-1}$ interval with values calculated from Eq. 26 and invert Eq. 22 to determine the VDOS $D(\bar{\nu})$ from the corrected excitation probability $S'(\bar{\nu})$, as well as the corresponding Fe MSD (Eq. 14) and resilience (Eq. 18). To avoid underestimating the recoilless fraction f in Eq. 22, we adjusted negative energy values to satisfy the detailed balance condition $S(-\bar{\nu}) = S(\bar{\nu})\exp[-hc\bar{\nu}/k_B T]$ for the purpose of calculating the integral in Eq. 24.

MD simulations

The computational protocol follows closely that developed by Zhang et al. (59) and Bu and Straub (60,61). The horse heart cyt *c* (or sperm whale myoglobin) molecule and solvent water were introduced into a $71.07 \times 71.07 \times 54.55 \text{ \AA}^3$ ($71.19 \times 71.19 \times 54.96 \text{ \AA}^3$) rectangular box and simulated using the CHARMM program (62). The initial configuration of the horse heart cyt *c* protein was taken from the Protein Data Bank to be the x-ray crystal structure at the oxidized form (PDB ID: 1HRC) (63). This structure is an oxidized form of cyt *c*, but it is also the highest resolution x-ray crystal structure for horse heart cyt *c* in the PDB. Because the difference between structures of the reduced and oxidized forms of cyt *c* is close to the limit of resolution of x-ray and NMR methods, we take 1HRC as our initial structure for both the oxidized and the reduced form of cyt *c*, then we use oxidized [Fe(III)] or reduced [Fe(II)] heme parameters in the CHARMM force field (64) to equilibrate the structure. The atom point charges of oxidized heme are taken from ab initio calculations (65). Partial charges used for both Fe(II) and Fe(III) heme are included as Supplementary Material, [Data S1](#) and [Data S2](#), respectively. The initial configuration of carbonmonoxy myoglobin was directly taken from the Protein Data Bank (PDB ID: 1MBC) (66), and deoxyMb was prepared by removing the carbon monoxide ligand. Upon this modification, the heme becomes pentacoordinated and the iron atom moves out of the porphyrin plane by roughly 0.3 \AA (67,68). The recently refined pentacoordinate heme parameters (69) were used to describe this domed heme structure. The initial configuration of the systems, including protein, heme, and solvent, was equilibrated at room temperature as part of a previous study (59–61). The all-hydrogen parameter set (Ver. 22) of the CHARMM force field (64) was used.

The equilibrium state of the protein in solution at room temperature was gradually cooled to 250 K, 200 K, 150 K, 100 K, 50 K, and 20 K, respectively. Subsequently, 20 ps of constant temperature molecular dynamics was run in which the temperature was checked every 0.2 ps for the first 10 ps and every 2.0 ps for the remaining 10 ps. The velocities were randomly re-sampled according to the Maxwell distribution to maintain a constant temperature. During the last 10-ps interval, the average temperature remained within a 5 K window and there was no need to resample the atomic velocities. At this point, it was assumed that an equilibrium state had been reached. The molecular dynamics employed the Verlet algorithm, which is time-reversible and symplectic (70–72), with a time step of 1 fs. Nonbonded terms in the potential were truncated using a group switching function extending from 9.5 to 11.5 Å. Molecular dynamics trajectories were then run for 60 ps at constant energy and volume for each temperature to simulate the dynamics in a frozen solution. Snapshots were saved every 10 steps.

Following a similar protocol, constant temperature and pressure trajectories were generated for each protein solution at 300 K. For each 60 ps trajectory, snapshots were saved every 10 fs.

Mean-squared displacements

In this subsection, we focus on the information about the heme dynamics, specifically the temperature dependence of the iron mean-squared displacement, as derived from computational and experimental results. The computational values result from calculating the Fe MSD by averaging over three 20-ps sections from each 60-ps trajectory and further averaging over the 10-trajectory ensemble.

Mössbauer spectroscopy may be used to measure the values of the electron density, the electric field gradient, and magnetic field of the iron atom in heme proteins, which can provide information about the symmetry and strength of the covalent bonds with the iron atom. (33,73–82) Previously published investigations (22,32,83–85) also used Mössbauer spectroscopy to determine the Fe MSD

$$\langle x^2 \rangle_\tau = -(\ln f)/k^2 = -\ln A/k^2 + \ln c/k^2 \quad (28)$$

of the ^{57}Fe atom as a function of temperature from the observed spectral area $A = cf$, which is proportional to the recoilless fraction f (Eq. 1). The vertical offset provided by the unknown proportionality constant c is adjusted to ensure that MSD values in a chosen temperature range extrapolate to $\langle x^2 \rangle_\tau = 0$ when $T \rightarrow 0$, as expected for a harmonic system (see Eq. 17 and accompanying discussion).

The resulting MSD values embody the assumption implicit in Eq. 1 that the Fe displacement has a Gaussian distribution, as expected for vibrational motion. The spectroscopic properties of the ^{57}Fe transition at $E_0 = 14.4 \text{ keV}$ provide suitable sensitivity to the length- and timescales of vibrational motions. The photon energy $E_0 = hck$ establishes a length scale $k^{-1} = 13.7 \text{ pm}$ that is comparable to the magnitude of Fe vibrational motion on picosecond timescales. The MSD values determined using Eq. 28 represent an average over the $\tau = 141 \text{ ns}$ lifetime of the ^{57}Fe nuclear excited state, which includes vibrational motion but may also include motions on longer timescales.

^{57}Fe NRVS measurements provide two means of characterizing the Fe MSD. The vibrational contribution $S'(\bar{\nu})$ to the excitation probability has an integrated area equal to $1-f$ (42). This directly determines values 0.79, 0.81, and 0.84 for the recoilless fractions f of Fe(II) cyt *c*, Fe(III) cyt *c*, and deoxyMb at the temperatures of the measurements. Through Eq. 28, this yields the MSD values plotted as individual points in Fig. 2.

Through the uncertainty principle, the energy resolution determines the timescale of motions that contribute to the NRVS measurements and thus to the resulting MSD values, with a 1 meV energy resolution corresponding to vibrations having periods 4 ps or shorter. Previous measurements show that MSD values determined from Mössbauer and from NRVS begin to deviate above $\sim 200 \text{ K}$, which was attributed to the activation of additional Fe motions on longer timescales above this temperature (58).

The VDOS determined from the measured excitation probability yields an estimate of the vibrational contribution to the MSD over the entire temperature range through Eq. 14. Fig. 2 shows that temperature-dependent values calculated in this way are consistent with the values determined from the excitation probability at the experimental temperature.

Let us consider sources of experimental uncertainty other than the central peak subtraction (whose effect is visible in Fig. 3). Random errors due to counting statistics contribute negligibly to the uncertainty in the vibrational MSD $\langle x^2 \rangle_v$, representing only 2% of $\langle x^2 \rangle_v$ for Fe(II) cyt *c* and 1.7% of $\langle x^2 \rangle_v$ for Fe(III) cyt *c*. The values chosen for the sample temperature and for the signal background entered into PHOENIX contribute more strongly to the experimental uncertainty.

Any temperature in a certain interval can be chosen to satisfy the consistency checks employed by PHOENIX (56). For example, temperatures chosen anywhere between 82 K and 95 K for Fe(II) cyt *c* satisfy detailed balance between Stokes and anti-Stokes signals within the experimental uncertainty. These temperature variations lead to corresponding variations $\delta D(\bar{\nu})$ in the low frequency region of $D(\bar{\nu})$ and therefore to different values for $\langle x^2 \rangle_v$. This temperature uncertainty is the primary systematic error contributing to the error bars in Fig. 2.

Detector noise or synchrotron timing errors contribute a weak energy-independent background B that is subtracted from the experimental signal to yield the pure nuclear resonance contribution, and there is some uncertainty in determining this background as well. We estimate this contribution from the signal level at high frequencies where there is no evidence of vibrational signals. Analysis of the experimental NRVs signal for frequencies higher than 528 cm^{-1} for oxidized cyt *c* (520 cm^{-1} for reduced) yields background levels $B = 4.09 \pm 0.27$ counts for Fe(III) and $B = 2.72 \pm 0.19$ counts for Fe(II) cyt *c*. The effect of these uncertainties on the Fe MSD, calculated from the VDOS using these variations in the background level input into PHOENIX, is less significant than for the temperature uncertainty. For example, for Fe(II) cyt *c*, $\langle x^2 \rangle_v = 43.7 \pm 0.7 \text{ pm}^2$ at the 87 K experimental temperature, based on the background uncertainty alone.

RESULTS

NRVS measurements were recorded at 87 K for Fe(II) cyt *c* and at 68 K for Fe(III) cyt *c*. Application of the analysis outlined in a previous section to these data, as well as to data previously recorded for deoxyMb (51), yielded the vibrational densities of states displayed in Fig. 4. The maximum near 30 cm^{-1} in deoxyMb was attributed to translation of the heme in response to global oscillations of the protein, rather than intraheme vibrations that dominate the Fe VDOS at higher frequencies (51). This feature is noticeably suppressed for cyt *c*. However, the oxidation state of cyt *c* has little influence on the Fe VDOS observed for cyt *c* in the $20\text{--}100 \text{ cm}^{-1}$ range. Vibrational changes among the three proteins are more apparent at frequencies above 200 cm^{-1} .

Fig. 2 reveals the temperature dependence of the vibrational contributions $\langle x^2 \rangle_v$ to the iron MSD, as predicted on the basis of the experimental VDOS. These MSD values are consistent with those determined from the excitation probability $S(\bar{\nu})$ at the experimental temperature. The slopes are significantly smaller for both reduced and oxidized cyt *c* than for the five-coordinate deoxyMb. Inspection of Fig. 4 suggests that the stronger T dependence results from an increased Fe VDOS for deoxyMb with respect to cyt *c* below 100 cm^{-1} , consistent with Eqs. 14 and 17.

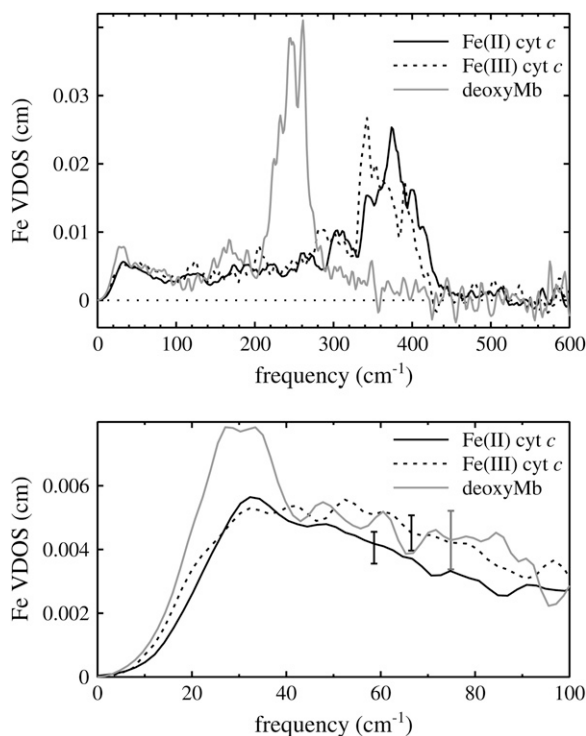


FIGURE 4 Experimentally determined VDOS for deoxyMb, Fe(II) cyt *c*, and Fe(III) cyt *c* over the full experimental frequency range (upper panel), and expanded to highlight frequencies below 100 cm^{-1} (lower panel). The cyt *c* VDOS is insensitive to oxidation state over the $[20, 100] \text{ cm}^{-1}$ interval, but the larger area in the deoxyMb spectrum in the latter region with respect to cyt *c* leads to a significantly larger Fe MSD at all temperatures (Fig. 2) and a lower resilience (Table 1).

To identify the frequencies that contribute most significantly to $\langle x^2 \rangle_v$, we plot the quantities $D(\bar{\nu})/\bar{\nu}$ and $D(\bar{\nu})/\bar{\nu}^2$ as functions of frequency (Fig. 5). Modes below 100 cm^{-1} constitute 87% of the integrated area of $D(\bar{\nu})/\bar{\nu}^2$ for Fe(II) cyt *c*, 88% for Fe(III) cyt *c*, and 89% for deoxyMb. Therefore, the low frequency vibrations dominate the high temperature behavior of the Fe mean-square displacement according to Eq. 17. However, modes below 100 cm^{-1} constitute only 45% of the integrated area of $D(\bar{\nu})/\bar{\nu}$ for Fe(II) cyt *c*, 48% for Fe(III) cyt *c*, and 49% for deoxyMb, indicating that the full spectrum of observed frequencies contributes to the zero-point motion of Fe (Eq. 20). Although vibrations with frequencies above 200 cm^{-1} dominate the observed vibrational density of states (Fig. 4), they contribute minimally to the mean-squared displacement of the iron at high temperature and will not be discussed further here.

Fig. 6 shows the temperature dependence of the $\langle x^2 \rangle_v$ values for Fe(II) and Fe(III) cyt *c*, derived from the molecular dynamics simulation results, together with simulated data for deoxyMb and MbCO calculated using a similar molecular dynamics method. Below 200 K, the simulations reveal qualitative trends in the temperature dependence of the Fe MSD similar to those determined from the experimental density of states (Fig. 2). The Fe MSD displays equivalent temperature vari-

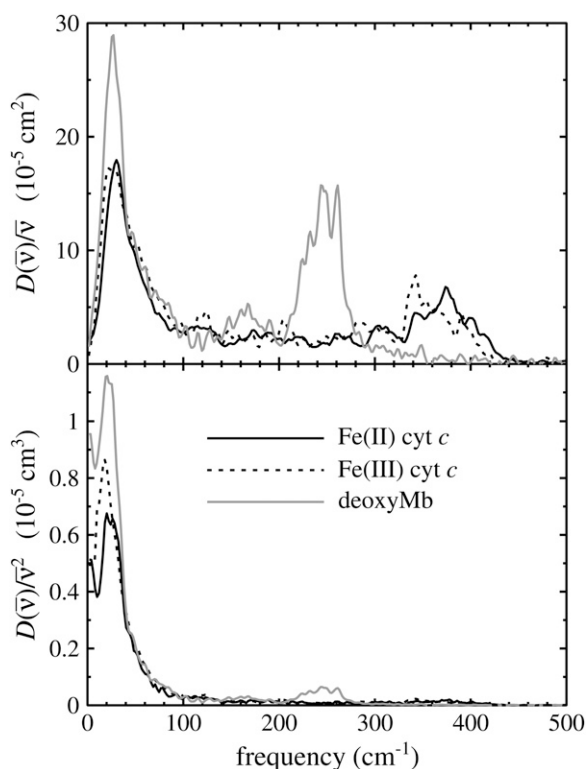


FIGURE 5 NRVs data for cyt *c* (solid) and deoxyMb (shaded) shown in terms of $D(\bar{\nu})/\bar{\nu}$ and $D(\bar{\nu})/\bar{\nu}^2$, respectively, to emphasize the vibrational modes that primarily contribute to the low and high temperature limiting values for the Fe MSD, as determined by Eqs. 20 and 17, respectively.

ation for the two oxidation states of cyt *c*, but increases significantly more rapidly with temperature for deoxyMb. In all cases, the Fe MSD increases rapidly above 200 K, as does the MSD of the heme, displayed as an inset to Fig. 6.

Fig. 7 compares the MSD prediction based on the experimental VDOS for horse Fe(II) and Fe(III) cyt *c* with experimental MSD values previously determined on the basis of Mössbauer spectroscopy for a sample containing a mixture of Fe(II) and Fe(III) *M. capsulatus* cyt *c* (22). The authors estimated the absolute MSD values by adjusting the additive constant *c* in Eq. 28 so that a linear extrapolation of points in the 100–200 K temperature range to $T = 0$ yields $\langle x^2 \rangle = 0$ (markers in Fig. 7). Above 200 K, the MSD values increase more rapidly, which is attributed to protein-specific motions (86) which occur on a timescale longer than 4 ps (1).

At lower temperatures, the MSD values increase almost linearly with temperature. Fig. 7 reveals quantitative agreement between the Fe MSD values derived from the experimental VDOS for horse Fe(III) cyt *c* and experimentally derived values reported for *M. capsulatus* Fe(III) cyt *c*. In contrast, the Fe MSD values derived from NRVS measurements for horse Fe(II) cyt *c* significantly exceed experimentally derived values reported for *M. capsulatus* Fe(II) cyt *c*. The slope of MSD as a function of temperature derived from the Mössbauer measurements is larger for Fe(III) cyt *c* than for the reduced protein by a factor of ~ 1.75 .

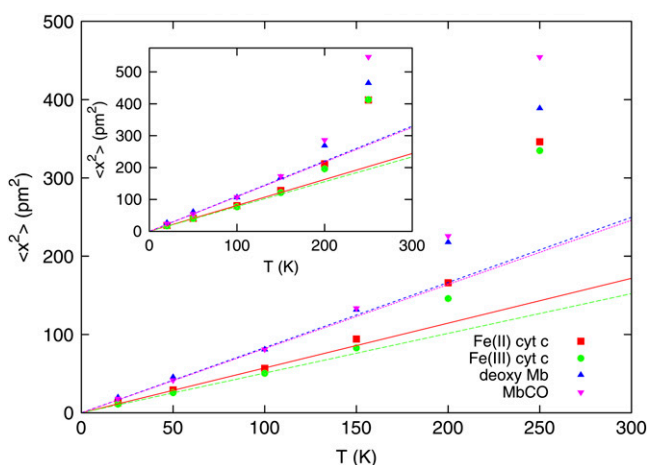


FIGURE 6 The simulated Fe MSD displays equivalent temperature variation for the two oxidation states of cyt *c*, but increases significantly more rapidly with temperature for deoxyMb and MbCO. Symbols represent the simulated Fe MSD for Fe(III) cyt *c*, Fe(II) cyt *c*, deoxyMb, and MbCO as a function of temperature. Slopes of least-square fitted solid lines determine the resilience values given in Table 1 according to Eq. 2. The inset displays the average MSD of the Fe and the 24 core atoms of the heme for the same four proteins.

Figs. 8–10 depict the MSD found for heme heavy atoms and for protein backbone atoms of cyt *c* and Mb, respectively, in simulations performed at six different temperatures. The MSD of other atoms also increase with temperature, qualitatively similar to the behavior predicted for the Fe atom. Above 200 K, the MSD of the backbone and heme peripheral atoms appear to be slightly larger than for the iron and the

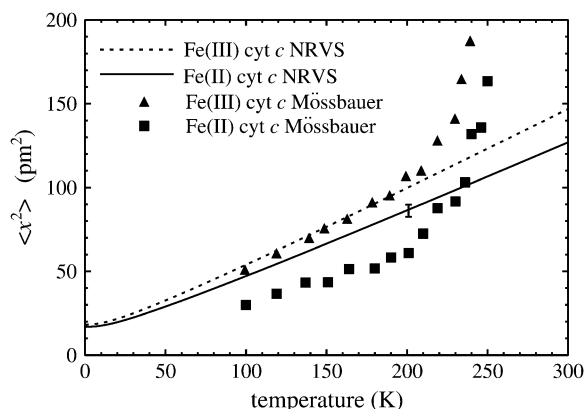


FIGURE 7 The Fe MSD of Fe(II) and Fe(III) cyt *c* as a function of temperature, as determined from the experimental VDOS (lines) and from Mössbauer experiments (markers). MSD values predicted from NRVS measurements on horse cyt *c* reported here are reproduced from Fig. 2. MSD values determined from Mössbauer measurements on *M. capsulatus* cyt *c* are obtained from Frolov et al. (22). There is nearly quantitative agreement for Fe(III) cyt *c*, but the Mössbauer results show MSD differences between oxidized and reduced cyt *c* substantially larger than those extrapolated from NRVS results.

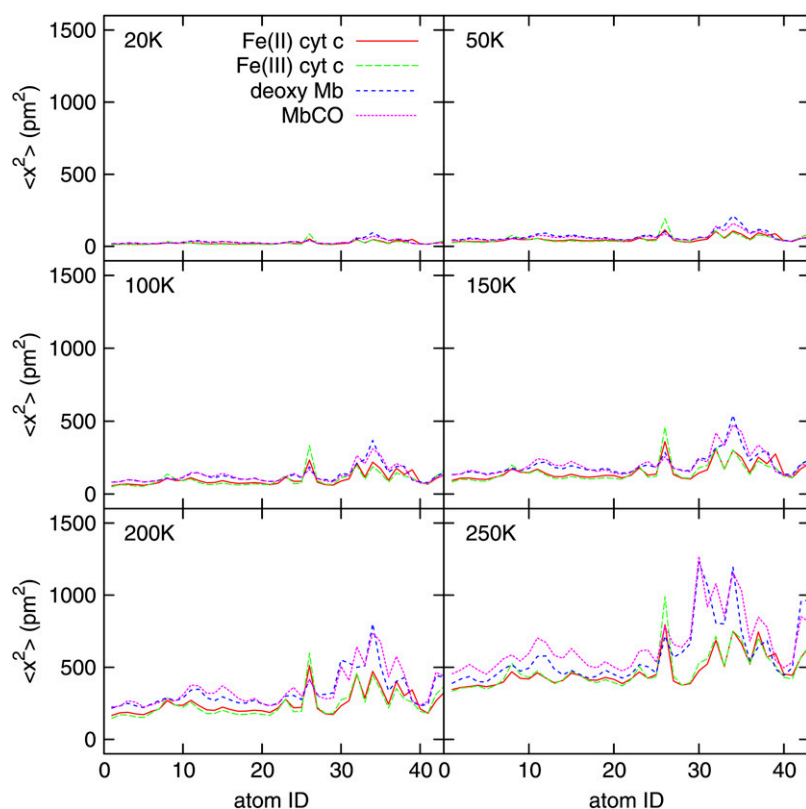


FIGURE 8 The MSD of heme heavy atoms (excluding hydrogen atoms) for Fe(II) cyt *c*, Fe(III) cyt *c*, deoxyMb, and MbCO, as predicted from MD simulations at variable temperature. With increasing temperature, the MSD also increases, but no significant difference between the MSD of heme heavy atoms in Fe(II) cyt *c* and Fe(III) cyt *c* is observed. Atom numbering follows the CHARMM residue topology file for the heme, with atoms numbered 1–25 corresponding to the iron and the 24 atoms of the heme core, respectively, and larger numbers referring to atoms of the peripheral groups.

24-atom heme core. In all cases, however, we observe no significant difference between the fluctuations of the reduced and oxidized forms of cyt *c*.

DISCUSSION

Resilience of the Fe environment

The resilience of the Fe environment defined in terms of the temperature variation of the Fe MSD according to Eq. 2 provides a convenient and intuitive basis for quantitative comparisons. Table 1 lists values of the resilience determined from NRVS measurements, from MD simulations, and from Mössbauer measurements.

The three independent determinations in Table 1 agree quantitatively for Fe(III) cyt *c*. However, discrepancies among the different methods exceed the estimated uncertainty for Fe(II) cyt *c* and for deoxyMb. Later sections will consider sources of systematic error that may account for differences in the absolute values determined experimentally for the resilience. Nevertheless, the results suggest that the CHARMM potential function is reasonably successful at reproducing the primary contributions to thermal displacements of the Fe at cryogenic temperatures. This contrasts with the reported difficulty at reproducing Fe vibrations above 100 cm^{-1} (87), which are likely to depend strongly on details of the CHARMM heme potential.

The concept of resilience was originally introduced (6) in the context of neutron scattering measurements, where experimental MSD values are averaged over a large number of atoms, with the primary contribution from hydrogens. Simulations suggest that the MSD, and thus the resilience, may vary from site to site within the protein (Figs. 9 and 10). As a result, experimental comparison of the resilience of the hydrogen sites with that of a specific atom at the active site carries some interest. Temperature-dependent neutron scattering data are not available for cyt *c*, but measurements on myoglobin below 200 K yield a value $k_r \simeq 8$ pN/pm for the average resilience of the hydrogen sites (27) that is significantly lower than the experimental values determined for the Fe site, as listed in Table 1. This indicates that the active site resilience may be larger than that of the average protein site.

This atom-specific resilience reflects differences between the Fe-weighted VDOS derived from NRVS measurements and the hydrogen-weighted VDOS determined from inelastic neutron scattering measurements. In particular, the Fe VDOS of Mb decreases above ~ 30 cm^{-1} (Fig. 4), while the reported H VDOS continues to increase monotonically up to 70 cm^{-1} (88). Quantitative comparison reveals that the H and Fe VDOS already begin to separate above 15 cm^{-1} (Fig. 12 in (58)). This difference between H and Fe sites was not apparent upon qualitative comparison of the experimental NRVS and inelastic neutron scattering signals (51), which both show maxima near 25 cm^{-1} .

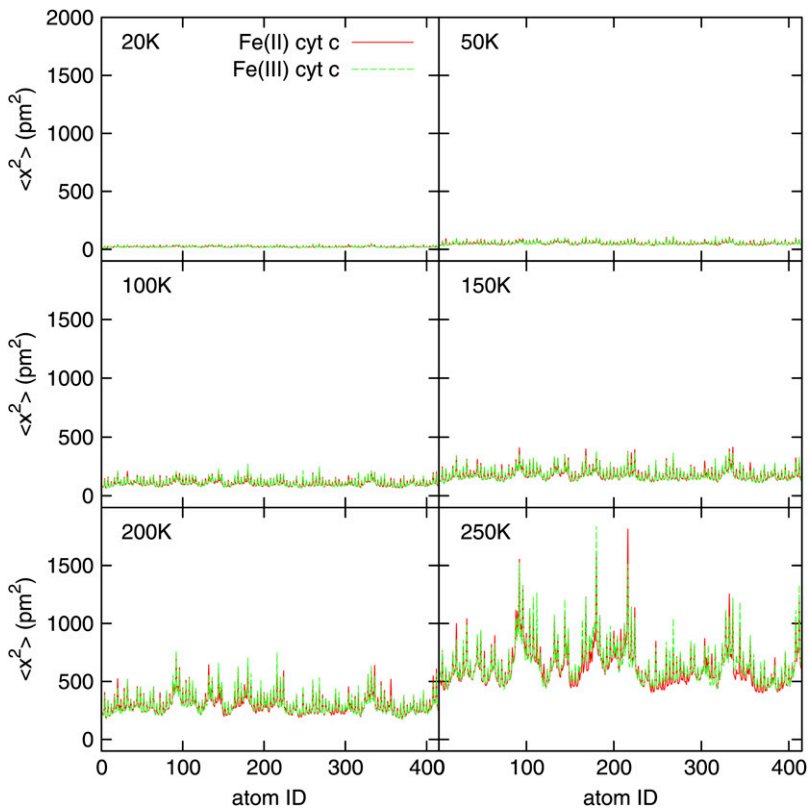


FIGURE 9 Simulated MSD for all protein backbone atoms for Fe(II) *cyt c* and Fe(III) *cyt c*. The MSD increases with increasing temperature, but there is no significant difference between the MSD of backbone atoms in Fe(II) *cyt c* and Fe(III) *cyt c*.

Vibrational contributions to the resilience

The MSD dependence on temperature extrapolated from the experimental Fe VDOS measured at a single temperature is nearly linear above 50 K (Fig. 2). Fe MSD values determined from Mössbauer measurements also vary linearly with temperature up to 200 K (22) (Fig. 7). For Fe(III) *cyt c*, consistency of the pure vibrational extrapolation with independent experimental and computational determinations directly confirms long-standing assumptions (3) that vibrational motion dominates the Fe MSD below 200 K, and further elucidates the nature of these vibrations. The lower panel of Fig. 5 displays the integrand of Eq. 17 and demonstrates that low frequency vibrations largely determine the temperature variation of the MSD. For the proteins measured here, we find that frequencies below 100 cm^{-1} account for 87–89% of the total area of the quantity $D_j(\bar{\nu})/\bar{\nu}^2$. We have previously suggested that net translation of the heme makes the primary contribution to the Fe vibrational signal in this frequency region (51). This is consistent with simulated dynamics, which find similar MSD values for the Fe atom and for the 24 core atoms of the heme (Fig. 8). Comparison of the three curves in the lower panel of Fig. 5 indicates that these motions are crucial determinants of variations in the resilience of the Fe site.

Mössbauer and neutron scattering measurements (22, 89,90) reveal that the resilience of both Fe sites (3,4) and H sites (5,6) decrease by as much as an order of magnitude above 200 K, where additional motions are activated. Pre-

vious results indicate that most of the additional Fe motion at high temperatures does not contribute to the NRVS signal and must take place on timescales slower than the 4 ps vibrational period corresponding to the 1 meV spectral resolution (58). Apparently, the Fe atom does not participate significantly in atomic motions responsible for the increased dielectric response on THz timescales observed above 200 K (91).

The simulations also reveal two distinct temperature regimes. In the low temperature regime ($<200\text{ K}$), the simulated MSD increases linearly with temperature for both reduced and oxidized forms of *cyt c*. In the high temperature regime ($>200\text{ K}$), the $\langle x^2 \rangle$ values begin to deviate from this linear behavior (Fig. 6). This phenomenon has been studied in previous computational investigations of proteins (92–94).

These results reinforce the accepted interpretation of this dynamical transition, in which two terms are considered to contribute to the total MSD

$$\langle x^2 \rangle = \langle x^2 \rangle_v + \langle x^2 \rangle_t. \quad (29)$$

The contribution $\langle x^2 \rangle_v$ results from quasiharmonic vibrational motion and is present at all temperatures. Additional contributions, $\langle x^2 \rangle_t$, result from protein-specific motions caused by thermally activated transitions of the protein between conformational substates, and only appear at high temperatures. This transition has often been interpreted in terms of a glass transition that occurs at a transition temperature T_c . However, existing computer simulations are too short to explore any

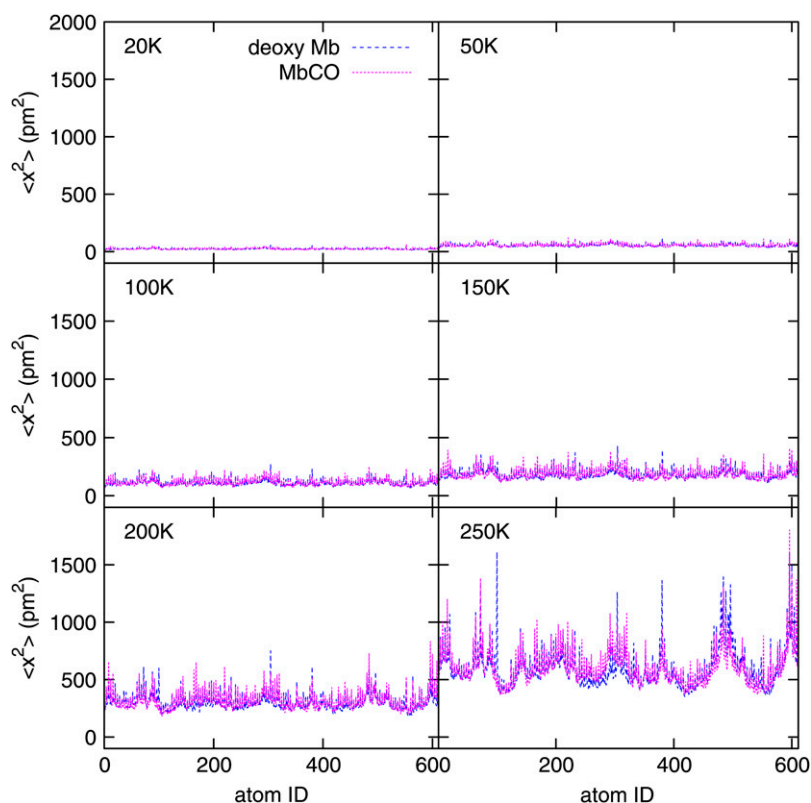


FIGURE 10 Simulated MSD for all protein backbone atoms for deoxyMb and MbCO. The MSD increases with increasing temperature, but there is no significant difference between the MSD of backbone atoms in deoxyMb and MbCO.

dynamical transition similar to transitions in glass-forming liquids (95).

Influence of thioether bridges

All theoretical and experimental methods find a larger resilience for the Fe site in *cyt c* than in deoxyMb (Table 1). This most likely reflects the altered heme-protein connectivity in *cyt c*. Apparently, the three additional linkages between the heme and the rest of the protein (the Fe-S(Met-80) bond and the two thioether links of Cys-14 and Cys-17 to the heme vinyl groups) restrict the mobility of the *cyt c* heme with respect to deoxyMb. These constraints on the heme reduce

the magnitude of the fluctuations of the central iron atom at a given temperature.

Qualitatively similar results are observed in NRVS measurements on cytochrome *f* (96), which also has thioether bridges covalently linking its heme to the protein. In this case, as well, the Fe VDOS is significantly reduced in comparison with deoxyMb at $<40\text{ cm}^{-1}$, as can be seen directly by comparing the lower panel of Fig. 4 to Fig. 6 in Adams et al. (96).

Mean force constants reported by Adams et al. (96), following analytical results by Lipkin (54), are proportional to the second moment $\langle \omega^2 \rangle$ of the VDOS, and thus are insensitive to this low frequency region. The resilience is a distinct quantity determined by the inverse second moment $\langle \omega^{-2} \rangle$ of the VDOS according to Eq. 18 and, as noted in the previous section, is dominated by frequencies below 100 cm^{-1} .

TABLE 1 Resilience determined for the Fe environment in heme proteins

Resilience (pN/pm)	Fe(II) <i>cyt c</i>	Fe(III) <i>cyt c</i>	deoxyMb	MbCO
Mössbauer	50	27	20	
NRVS	32.6(+1.6/-1.5)	28.3	20.9(+1.5/-1.1)	
Simulations	24.1 ± 0.4	27.2 ± 0.3	16.6 ± 0.7	16.8 ± 0.2

Values were determined from NRVS and MD simulations as described in the text. Temperature-dependent MSD values determined from Mössbauer results, as reported in Frolov et al. (22) for Fe(II) *cyt c* and Fe(III) *cyt c* (reproduced in Fig. 7) and in Achterhold et al. (58) for deoxyMb, determine additional values for resilience according to Eq. 2.

Influence of oxidation

We have devoted particular attention to the possibility that the resilience of the Fe environment depends on oxidation state, motivated by previous investigations of the influence of oxidation state on the structure and dynamics of *cyt c*. Equilibrium structures of reduced and oxidized *cyt c* show minimal differences, either in the crystalline phase (16,17,63, 97–99) or in solution (18,19,100–102). Crystal structures are available only for the oxidized state of horse *cyt c* (63,99), and the significance of small structural differences between

oxidized and reduced tuna cyt *c* (97,98) is unclear because they crystallize in different lattices. However, the root mean-square (RMS) displacement between backbone atoms is only 30 pm between oxidized and reduced structures of a mitochondrial cyt *c* from yeast in isomorphous crystals (17). Structures of horse cyt *c* in solution derived from NMR measurements reveal a slightly larger 140 pm RMS deviation between backbone atoms in oxidized and reduced states (18,19).

Early small angle x-ray scattering studies were interpreted as evidence for an increased radius of gyration for the oxidized state in low ionic strength solution (103). However, more recent analysis of x-ray scattering from cyt *c* solutions attributed differences in the small angle signal to interparticle interactions, which are screened more effectively at higher ionic strength (104). Consistent with this result, a crystal structure of oxidized cyt *c* at low ionic strength (99) resembles that determined at high salt concentration.

In contrast to the small structural changes, numerous studies find increased chemical reactivity of cyt *c* upon oxidation, which is often attributed to an increase in “flexibility” (20). Physical investigations have not reached a consensus on the dynamical processes contributing to the increased “flexibility” of the oxidized state. Early neutron scattering measurements recorded for both Fe(II) and Fe(III) cyt *c* showed no significant differences, leading to the conclusion (105) that oxidation had little effect on the dynamics of cyt *c*, at least on the timescales probed by these measurements (105).

More recent measurements have revived interest in possible dynamical changes upon oxidation. Frolov et al. (22) studied the dynamics of a bacterial cyt *c* using Mössbauer spectroscopy. They measured the dependence of the iron MSD on temperature and found that the slope in the oxidized state was significantly higher than in the reduced state (see the previous subsection as well as Fig. 7). Chen et al. (23) used THz spectroscopy to probe the dielectric response of bovine cyt *c*, reporting an increase in the absorption coefficient in Fe(III) cyt *c* by 70–100% with respect to Fe(II) cyt *c* at ambient temperature. On the other hand, Chin et al. (24) monitored the C-D stretching frequency of the selectively

deuterated Met-80 heme ligand in Fe(II) and Fe(III) cyt *c*. Their results suggest that heme dynamics is not affected by changes in the oxidation state. In more recent results from this group (106), they report the incorporation of carbon-deuterium bonds throughout cyt *c* and characterize their absorption frequencies and linewidths using IR spectroscopy. Analysis of these data indicates the presence of locally unfolded regions in the oxidized protein.

The NRVS and MD results presented here yield temperature-dependent MSD values that compare quantitatively with the results reported by Frolov et al. for Fe(III) cyt *c* (Fig. 7) (22). On the other hand, we find that the oxidation state has much less influence on the temperature-dependent MSD (expressed in terms of resilience in Table 1) than reported for the Mössbauer measurements. MSD and resilience values determined for Fe(II) cyt *c* using both NRVS experiments and MD simulations exceed those determined from Mössbauer experiments for all temperatures below 230 K. In the simulations, the dynamics of other atoms also appear independent of oxidation state (Fig. 8).

Although the Mössbauer measurements were carried out in lower ionic strength solutions (5 mM phosphate, pH 7.4) than the NRVS measurements (0.1 M phosphate buffer, pH 7.4), this is unlikely to account for the observed discrepancy. Significant structural differences are not observed for horse cyt *c* crystals grown at differing ionic strengths (63,99).

The Mössbauer measurements were performed on cyt *c* obtained from a bacterial source (*Methylococcus capsulatus*), and it is conceivable that the prokaryotic protein exhibits different dynamical behavior that would account for the apparent discrepancy with the results reported here. We have identified a 129-amino-acid coding sequence from the *M. capsulatus* genome (107) that aligns with the four heme-binding residues of the 104-amino-acid sequence of horse heart cyt *c* (Table 2). However, the modest overall sequence similarity, together with an additional N-terminal segment, might lead to distinct dynamical properties.

In the THz study cited above (23), the authors attribute the increased absorption coefficient in bovine Fe(III) cyt *c* with respect to Fe(III) cyt *c* to an increase in vibrational mode

TABLE 2 CLUSTAL W multiple sequence alignment for cytochromes *c*

sp XP_583465 CYC_COW	-----MGDVEKGGKIFVQKCAQCHTVEKGGKHK	29
sp P00004 CYC_HORSE	-----GDVEKGGKIFVQKCAQCHTVEKGGKHK	28
sp AAU92773 CYC_BATH	MNVRRLDLGCGVVLALAAGAAYAGDVAAG-KTKYERCVECHGRGEGDAAPN	51
	*** * * :*:** :*	
sp XP_583465 CYC_COW	GPNLHGLFGRKTGQAPG-FSYTDANKNKGITWGEETLMEYLENPKKYIPG	79
sp P00004 CYC_HORSE	GPNLHGLFGRKTGQAPG-FTYTDANKNKGITWKEETLMEYLENPKKYIPG	78
sp AAU92773 CYC_BATH	VPFLAGKDSNYIRRVLNTYKRCRPDDWLPCCGGSEERIQQPFWEHRSKDG	103
	. * .. :. :. :. :. * : : : *	
sp XP_583465 CYC_COW	M-IFAGIKKKGEREDLIAYLKATNE	105
sp P00004 CYC_HORSE	M-IFAGIKKKTEREDLIAYLKATNE	104
sp AAU92773 CYC_BATH	MREIASLSDTDIDDLAAYIATFRKP	129
	* :* . . : :** **: . :	

Top, middle, and bottom rows list sequences from cow, horse, and *M. capsulatus*, respectively. Note alignment of the amino acids that covalently bind the heme: Cys-14, Cys-17, His-18, and Met-80 in the sequence from horse.

density below 80 cm^{-1} . In contrast, we find the Fe VDOS of oxidized and reduced cyt *c* to be indistinguishable below 80 cm^{-1} (Figs. 2 and 7). Furthermore, the amino acid sequence of cyt *c* from horse differs from cow at only three positions (Table 2) (108). Thus, the differences observed in this frequency region in THz experiments must be attributed to motions taking place in regions distant from the heme. One possibility is that surface residues and hydration water contribute disproportionately to the polarizability in this frequency region. Recent data published by Sagle et al. (106) suggest that parts of cyt *c* exist in dynamic equilibrium with locally unfolded states and that, for some residues, the degree of unfolding depends on the protein's oxidation state.

Compressibility

Fluctuations of the system volume determine the isothermal bulk compressibility

$$\beta_T = \frac{\overline{\delta V^2}}{k_B T V}, \quad (30)$$

an additional mechanical property of interest (109). Molecular dynamics simulations at constant pressure and temperature yield the RMS volume fluctuation δV . Tables 3 and 4 summarize the volume V , δV , and the calculated isothermal compressibility for the whole system and for the protein, respectively, resulting from our simulations at atmospheric pressure and $T = 300 \text{ K}$. The Voronoi volumes for protein and heme were used as the protein volume, which was calculated using the program Code-Mbg (110,111). The calculated isothermal compressibility for the entire protein solution system is very close to the experimentally measured value of 0.45 GPa^{-1} for bulk water (112), indicating the dominant contribution of the solvent.

Experimental investigations have estimated intrinsic compressibilities in the $0.10\text{--}0.25 \text{ GPa}^{-1}$ range for a number of proteins (113). Based on measured densities and sound velocities in cyt *c* solutions, and making assumptions regarding the relative contributions of bulk water, hydration water, and protein, Eden et al. (114) estimated that the oxidized protein had a 67% higher adiabatic compressibility than the reduced protein. However, this factor was determined to be just 2% in a later study (115). It can be difficult to distinguish the relative contributions of protein and solvent to bulk properties such as β_T (22). However, we find no sig-

TABLE 3 Isothermal compressibilities determined for Fe(II) cyt *c*, Fe(III) cyt *c*, deoxyMb, and MbCO solutions from MD simulations

Protein	V (\AA^3)	$\overline{\delta V}$ (\AA^3)	β_T (GPa^{-1})
Fe(II) cyt <i>c</i>	275,589.96	699.62	0.43
Fe(III) cyt <i>c</i>	275,506.14	671.19	0.40
deoxyMb	275,090.43	669.15	0.40
MbCO	275,978.01	681.26	0.41

TABLE 4 Isothermal compressibilities determined for Fe(II) cyt *c*, Fe(III) cyt *c*, deoxyMb, and MbCO proteins from MD simulations

Protein	V (\AA^3)	$\overline{\delta V}$ (\AA^3)	β_T (GPa^{-1})
Fe(II) cyt <i>c</i>	15,919.25	80.81	0.10
Fe(III) cyt <i>c</i>	15,931.19	81.31	0.10
deoxyMb	23,487.09	107.60	0.12
MbCO	23,487.93	106.60	0.12

nificant influence of the protein oxidation state on the compressibility of the concentrated protein/solvent systems simulated here.

CONCLUSIONS

The experimental and computational approaches utilized here reveal a consistent picture of how protein structure affects the mechanical properties of the heme environment. Below 200 K , vibrational motion in the THz region ($\bar{\nu} \leq 100 \text{ cm}^{-1}$) forms the primary contribution to the Fe MSD. Translation of the heme core is likely to dominate this motion. The Fe oxidation state has little influence on the resilience of the Fe environment in horse cyt *c*. However, the additional covalent connections between the heme and the protein enhance the local resilience in cyt *c* as compared with the more loosely bound heme in Mb.

SUPPLEMENTARY MATERIAL

To view all of the supplemental files associated with this article, visit www.biophysj.org.

We thank Tom H. Ching for assistance with reconstitution of cytochrome *c* and Prof. Abel Schejter for useful discussions. MD simulations were carried out at Boston University's Center for Computer Science.

We acknowledge generous support of this research by the National Science Foundation (grant Nos. PHY-0545787 to J.T.S. and CHE-9975494 and CHE-0316551 to J.E.S.). Use of the Advanced Photon Source was supported by the U.S. Department of Energy, Basic Energy Sciences, Office of Science, under contract No. DE-AC02-06CH11357.

REFERENCES

1. Parak, F. G. 2003. Physical aspects of protein dynamics. *Rep. Prog. Phys.* 66:103–129.
2. Frauenfelder, H., G. A. Petsko, and D. Tsemoglou. 1979. Temperature-dependent x-ray diffraction as a probe of protein structural dynamics. *Nature*. 280:558–563.
3. Keller, H., and P. G. Debrunner. 1980. Evidence for conformational and diffusional mean square displacements in frozen aqueous solution of oxymyoglobin. *Phys. Rev. Lett.* 45:68–71.
4. Parak, F., and E. W. Knapp. 1984. A consistent picture of protein dynamics. *Proc. Natl. Acad. Sci. USA.* 81:7088–7092.
5. Doster, W., S. Cusack, and W. Petry. 1989. Dynamical transition of myoglobin revealed by inelastic neutron scattering. *Nature*. 337:754–756.

6. Zaccai, G. 2000. How soft is a protein? A protein dynamics force constant measured by neutron scattering. *Science*. 288:1604–1607.
7. Austin, R. H., K. W. Beeson, L. Eisenstein, H. Frauenfelder, and I. C. Gunsalus. 1975. Dynamics of ligand binding to myoglobin. *Biochemistry*. 14:5355–5373.
8. van Thor, J., G. Y. Georgiev, M. Towrie, and J. T. Sage. 2005. Ultrafast and low barrier motions in the photoreactions of the green fluorescent protein. *J. Biol. Chem.* 280:33652–33659.
9. Rasmussen, B. F., A. M. Stock, D. Ringe, and G. A. Petsko. 1992. Crystalline ribonuclease a loses function below the dynamical transition at 220 K. *Nature*. 357:423–424.
10. Daniel, R. M., J. C. Smith, M. Ferrand, S. Hery, R. Dunn, and J. L. Finney. 1998. Enzyme activity below the dynamical transition at 220 K. *Biophys. J.* 75:2504–2507.
11. Tarek, M., and D. J. Tobias. 2002. Role of protein-water hydrogen bond dynamics in the protein dynamical transition. *Phys. Rev. Lett.* 88:138101.
12. Fenimore, P. W., H. Frauenfelder, B. H. McMahon, and F. G. Parak. 2002. Slaving: solvent fluctuations dominate protein dynamics and functions. *Proc. Natl. Acad. Sci. USA*. 99:16047–16051.
13. Sacquin-Mora, S., and R. Lavery. 2006. Investigating the local flexibility of functional residues in hemoproteins. *Biophys. J.* 90:2706–2717.
14. Sage, J. T. 2004. Hemoglobins: O₂ uptake and transport. In *Encyclopedia of Supramolecular Chemistry*, Marcel-Dekker, New York.
15. Scott, R. A., and A. G. Mauk. 1995. *Cytochrome c: A Multidisciplinary Approach*. University Science Books, Sausalito, CA.
16. Louie, G. V., and G. D. Brayer. 1990. High-resolution refinement of yeast iso-1-cytochrome c and comparisons with other eukaryotic cytochromes c. *J. Mol. Biol.* 214:527–555.
17. Berghuis, A. M., and G. D. Brayer. 1992. Oxidation state-dependent conformational changes in cytochrome c. *J. Mol. Biol.* 223:959–976.
18. Banci, L., I. Bertini, H. B. Gray, C. Luchinat, T. Reddig, A. Rosato, and P. Turano. 1997. Solution structure of oxidized horse heart cytochrome c. *Biochemistry*. 36:9867–9877.
19. Banci, L., I. Bertini, J. G. Huber, G. A. Spyroulias, and P. Turano. 1999. Solution structure of reduced horse heart cytochrome c. *J. Biol. Inorg. Chem.* 4:21–31.
20. Schejter, A. 1996. Oxidation state-dependent properties of cytochrome c. In *Cytochrome c: A Multidisciplinary Approach*, Chapt. 8. University Science Books, Sausalito, CA.
21. Cheng, M.-C., A. M. Rich, R. S. Armstrong, P. J. Ellis, and P. A. Lay. 1999. Determination of iron-ligand bond lengths in ferric and ferrous horse heart cytochrome c using multiple-scattering analyses of XAFS data. *Inorg. Chem.* 38:5703–5708.
22. Frolov, E. N., R. Gvodsev, V. I. Goldanskii, and F. G. Parak. 1997. Differences in the dynamics of oxidized and reduced cytochrome c measured by Mössbauer spectroscopy. *J. Biol. Inorg. Chem.* 2:710–713.
23. Chen, J. Y., J. R. Knab, J. Cerne, and A. G. Markelz. 2005. Large oxidation dependence observed in terahertz dielectric response for cytochrome c. *Phys. Rev. E Stat. Nonlin. Soft Matter Phys.* 72:040901.
24. Chin, J. K., R. Jimenez, and F. E. Romesberg. 2002. Protein dynamics and cytochrome c: correlations between ligand vibrations and redox activity. *J. Am. Chem. Soc.* 124:1846–1847.
25. Sturhahn, W. 2004. Nuclear resonant spectroscopy. *J. Phys. Condens. Matter*. 16:S497–S530.
26. Sage, J. T., C. Paxson, G. R. A. Wyllie, W. Sturhahn, S. M. Durbin, P. M. Champion, E. E. Alp, and W. R. Scheidt. 2001. Nuclear resonance vibrational spectroscopy of a protein active-site mimic. *J. Phys. Condens. Matter*. 13:7707–7722.
27. Bicout, D. J., and G. Zaccai. 2001. Protein flexibility from the dynamical transition: a force constant analysis. *Biophys. J.* 80:1115–1123.
28. Garcia, A. E., J. A. Krumhansl, and H. Frauenfelder. 1997. Variations on a theme by Debye and Waller: from simple crystals to proteins. *Proteins Struct. Funct. Genet.* 29:153–160.
29. Drenth, J. 2007. *Principles of Protein X-Ray Crystallography*, 3rd Ed. Springer-Verlag, New York.
30. Greenwood, N. N., and T. C. Gibb. 1971. *Mössbauer Spectroscopy*. Chapman and Hall, London, UK.
31. Cranshaw, T. E., B. W. Dale, G. O. Longworth, and C. E. Johnson. 1985. *Mössbauer Spectroscopy and its Applications*. Cambridge University Press, Cambridge, UK.
32. Parak, F., and L. Reinisch. 1986. Mössbauer effect in the study of structure dynamics. *Methods Enzymol.* 131:568–607.
33. Chen, Y.-L., and D.-P. Yang. 2007. *Mössbauer Effect in Lattice Dynamics: Experimental Techniques and Applications*. Wiley-VCH, New York.
34. Smith, J. C. 1991. Protein dynamics: comparison of simulations with inelastic neutron scattering experiments. *Q. Rev. Biophys.* 24:227–291.
35. Gabel, F., D. Bicout, U. Lehnert, M. Tehei, M. Weik, and G. Zaccai. 2002. Protein dynamics studied by neutron scattering. *Q. Rev. Biophys.* 35:327–367.
36. Weiss, T. M., P.-J. Chen, H. Sinn, E. E. Alp, S.-H. Chen, and H. W. Huang. 2003. Collective chain dynamics in lipid bilayers by inelastic x-ray scattering. *Biophys. J.* 84:3767–3776.
37. Angelini, T. E., R. Golestanian, R. H. Coridan, J. C. Butler, A. Beraud, M. Krisch, H. Sinn, K. S. Schweizer, and G. C. Wong. 2006. Counterions between charged polymers exhibit liquid-like organization and dynamics. *Proc. Natl. Acad. Sci. USA*. 103:7962–7967.
38. Parak, F., E. W. Knapp, and D. Kucheida. 1982. Protein dynamics: Mössbauer spectroscopy on deoxymyoglobin crystals. *J. Mol. Biol.* 161:177–194.
39. William, D. Callister, J. 2006. *Materials Science and Engineering: An Introduction*, 7th Ed. Wiley, New York.
40. Merzbacher, E. 1997. *Quantum Mechanics*, 3rd Ed. Wiley, New York.
41. Cohen-Tannoudji, C., B. Diu, and F. Laloe. 1977. *Quantum Mechanics*. Wiley, New York.
42. Leu, B. M. 2006. Nuclear resonance vibrational spectroscopy: a quantitative picture of iron dynamics in heme proteins and model compounds. PhD thesis, Northeastern University, Boston, MA.
43. Vanderkooi, J. M., and M. Erecinska. 1975. Cytochrome c interaction with membranes. *Eur. J. Biochem.* 60:199–207.
44. Robinson, A. B., and M. D. Kamen. 1968. Some observations on the use of hydrogen fluoride in cytochrome degradation and synthesis. *Struct. Funct. Cytochromes Proc. Symp.* 1967, University Park Press, Baltimore, MD.
45. Fisher, W. R., H. Taniuchi, and C. B. Anfinsen. 1973. On the role of heme in the formation of the structure of cytochrome c. *J. Biol. Chem.* 248:3188–3195.
46. Morell, D. B., and M. Stewart. 1956. The removal of iron from hemins. *Aust. J. Exp. Biol. Med. Sci.* 34:211–217.
47. Warburg, O., and E. Negelein. 1932. Hemin of the oxygen-transferring respiratory enzyme, some artificial hemoglobins and Spirographis porphyrin. *Biochem. Z.* 244:9–32.
48. Flatmark, T., and A. B. Robinson. 1968. Circular dichroic absorption spectra of cytochrome c from bovine heart and cytochrome c2 from *Rhodospirillum rubrum*. *Struct. Funct. Cytochromes Proc. Symp.* 1967, University Park Press, Baltimore, MD.
49. Koch, S. A. 1975. Iron macrocycle complexes. PhD thesis, Massachusetts Institute of Technology, Boston, MA.
50. Hardt, V. H. D., and W. Möller. 1961. On the solvent-free iron(II)-acetate. *Z. Anorg. Allg. Chem.* 313:57–69.
51. Sage, J. T., S. M. Durbin, W. Sturhahn, D. C. Wharton, P. M. Champion, P. Hession, J. Sutter, and E. E. Alp. 2001. Long-range reactive dynamics in myoglobin. *Phys. Rev. Lett.* 86:4966–4969.
52. Teale, F. W. J. 1959. Cleavage of the heme-protein link by acid methylethylketone. *Biochim. Biophys. Acta.* 35:543–550.
53. Zeng, W., N. J. Silvernail, W. R. Scheidt, and J. T. Sage. 2007. Nuclear Resonance Vibrational Spectroscopy (NRVS). Applications

- of Physical Methods to Inorganic and Bioinorganic Chemistry. Wiley, Chichester, UK.
54. Lipkin, H. J. 1995. Mössbauer sum rules for use with synchrotron sources. *Phys. Rev. B*. 52:10073–10079.
 55. Sturhahn, W., T. S. Toellner, E. E. Alp, X. Zhang, M. Ando, Y. Yoda, S. Kikuta, M. Seto, C. W. Kimball, and B. Dabrowski. 1995. Phonon density of states measured by inelastic nuclear resonant scattering. *Phys. Rev. Lett.* 74:3832–3835.
 56. Sturhahn, W. 2000. CONUSS and PHOENIX: evaluation of nuclear resonant scattering data. *Hyp. Intl.* 125:149–172.
 57. Johnson, D. W., and J. C. H. Spence. 1974. Determination of the single-scattering probability distribution from plural-scattering data. *J. Phys. D*. 7:771–780.
 58. Achterhold, K., C. Keppler, A. Ostermann, U. van Bürck, W. Sturhahn, E. E. Alp, and F. G. Parak. 2002. Vibrational dynamics of myoglobin determined by the phonon-assisted Mössbauer effect. *Phys. Rev. E Stat. Nonlin. Soft Matter Phys.* 65:051916.
 59. Zhang, Y., H. Fujisaki, and J. E. Straub. 2007. Molecular dynamics study on the solvent dependent heme cooling following ligand photolysis in carbonmonoxy myoglobin. *J. Phys. Chem. B*. 111:3243–3250.
 60. Bu, L., and J. E. Straub. 2003. Vibrational frequency shifts and relaxation rates for a selected vibrational mode in cytochrome *c*. *Biophys. J.* 85:1429–1439.
 61. Bu, L., and J. Straub. 2003. Simulating vibrational energy flow in proteins: relaxation rate and mechanism for heme cooling in cytochrome *c*. *J. Phys. Chem. B*. 107:12339–12345.
 62. Brooks, B. R., R. Bruccoleri, B. Olafson, D. States, S. Swaminathan, and M. Karplus. 1983. CHARMM: a program for macromolecular energy, minimization and dynamics calculations. *J. Comput. Phys.* 4:187–217.
 63. Bushnell, G. W., G. V. Louie, and G. D. Brayer. 1990. High-resolution three-dimensional structure of horse heart cytochrome *c*. *J. Mol. Biol.* 214:585–595.
 64. MacKerell, A. D., Jr., D. Bashford, M. Bellott, R. L. Dunbrack, Jr., J. Evansack, M. Field, S. Fischer, J. Gao, H. Guo, S. Ha, D. Joseph-McCarthy, L. Kuchnir, K. Kuczera, F. Lau, C. Mattos, S. Michnick, T. Ngo, D. Nguyen, B. Prodhom, I. W. E. Reiher, B. Roux, M. Schlenkrich, J. Smith, R. Stote, J. E. Straub, M. Watanabe, J. Wioorkiewicz-Kuczera, D. Yin, and M. Karplus. 1998. All-atom empirical potential for molecular modeling and dynamics studies of proteins. *J. Phys. Chem. B*. 102:3586–3616.
 65. Banci, L., G. Gori-Savellini, and P. Turano. 1997. A molecular dynamics study in explicit water of the reduced and oxidized forms of yeast iso-1-cytochrome *c*: solvation and dynamics properties of the two oxidized states. *Eur. J. Biochem.* 249:716–723.
 66. Kuriyan, J., S. Wilz, M. Karplus, and G. A. Petsko. 1986. X-ray structure and refinement of carbon-monooxy (Fe-II)-myoglobin at 1.5 Å resolution. *J. Mol. Biol.* 192:133–154.
 67. Kachalova, G. S., A. N. Popov, and H. D. Bartunik. 1999. A steric mechanism for inhibition of CO binding to heme proteins. *Science*. 284:473–476.
 68. Schlichting, I., J. Berendzen, G. N. Phillips, Jr., and R. M. Sweet. 1994. Crystal structure of photolyzed carbonmonooxy-myoglobin. *Nature*. 371:808–812.
 69. Meuwly, M., O. M. Becker, R. Stote, and M. Karplus. 2002. NO rebinding to myoglobin: a reactive molecular dynamics study. *Biophys. Chem.* 98:183–207.
 70. Verlet, L. 1967. Computer “experiments” on classical fluids. I. Thermodynamical properties of Lennard-Jones molecules. *Phys. Rev.* 159:98–103.
 71. Tuckerman, M., B. Berne, and G. Martyna. 1992. Reversible multiple time scale molecular dynamics. *J. Chem. Phys.* 97:1990–2001.
 72. Frenkel, D., and B. Smit. 2001. Understanding Molecular Simulation: From Algorithms to Applications, 2nd Ed. Academic Press, San Diego, CA.
 73. Kauffmann, K., C. Goddard, A. Christine, Y. Zang, R. Holm, and E. Munck. 1997. Mössbauer and magnetization studies of heme-copper-bridged assemblies pertinent to cytochrome *c* oxidase. *Inorg. Chem.* 36:985–993.
 74. Pereira, I. A. C., J. LeGall, A. V. Xavier, and M. Teixeira. 1997. The membrane-bound high-molecular-mass cytochromes *c* from *Desulfovibrio gigas* and *Desulfovibrio vulgaris* Hildenborough; EPR and Mössbauer studies. *J. Biol. Inorg. Chem.* 2:23–31.
 75. Prazeres, S., J. J. Moura, I. Moura, R. Gilmour, C. F. Goodhew, G. W. Pettigrew, N. Ravi, and B. H. Huynh. 1995. Mössbauer characterization of *Paracoccus denitrificans* cytochrome *c* peroxidase: further evidence for redox and calcium binding-induced heme-heme interaction. *J. Biol. Chem.* 270:24264–24269.
 76. Wang, H., T. Sauke, P. Debrunner, and S. Chan. 1988. The CO adduct of yeast cytochrome *c* oxidase: Mössbauer and photolysis studies. *J. Biol. Chem.* 263:15260–15263.
 77. Kent, T., L. Young, G. Palmer, J. Fee, and E. Munck. 1983. Mössbauer study of beef heart cytochrome oxidase: comparative study of the bovine enzyme and cytochrome *c*_{1aa3} from *Thermus thermophilus*. *J. Biol. Chem.* 258:8543–8546.
 78. Baumgartner, C. P., M. Sellers, R. Nassif, and L. May. 1974. Mössbauer studies of some complexes of the undecapeptide of cytochrome *c*. *Eur. J. Biochem.* 46:625–629.
 79. Cooke, R., and P. Debrunner. 1968. Mössbauer studies of the iron atom in cytochrome *c*. *J. Chem. Phys.* 48:4532–4537.
 80. Lang, G., D. Herbert, and T. Yonetani. 1968. Mössbauer spectroscopy of cytochrome *c*. *J. Chem. Phys.* 49:944–950.
 81. Havlin, R. H., N. Godbout, R. Salzmann, M. Wojdelski, W. Arnold, C. E. Schulz, and E. Oldfield. 1998. An experimental and density functional theoretical investigation of iron-57 Mössbauer quadrupole splittings in organometallic and heme-model compounds: applications to carbonmonooxy-heme protein structure. *J. Am. Chem. Soc.* 120:3144–3151.
 82. Ravi, N., I. Moura, C. Costa, M. Teixeira, J. LeGall, J. J. Moura, and B. H. Huynh. 1992. Mössbauer characterization of the tetraheme cytochrome *c*₃ from *Desulfovibrio baculatus* (DSM 1743): spectral deconvolution of the heme components. *Eur. J. Biochem.* 204:779–782.
 83. Melchers, B., E. Knapp, F. Parak, L. Cordone, A. Cupane, and M. Leone. 1996. Structural fluctuations of myoglobin from normal-modes, Mössbauer, Raman, and absorption spectroscopy. *Biophys. J.* 70:2092–2099.
 84. Lichtenegger, H., W. Doster, T. Kleinert, A. Birk, B. Sepio, and G. Vogl. 1999. Heme-solvent coupling: a Mössbauer study of myoglobin in sucrose. *Biophys. J.* 76:414–422.
 85. Jørgensen, A. M., F. Parak, and H. E. M. Christensen. 2005. Reduced and oxidized cytochrome *c*₄ exhibit differences in dynamics. *Phys. Chem. Chem. Phys.* 7:3472–3477.
 86. Frauenfelder, H., F. Parak, and R. D. Young. 1988. Conformational substates in proteins. *Ann. Rev. Biophys. Chem.* 17:451–479.
 87. Rai, B., E. Prohofsky, and S. Durbin. 2005. Single-atom test of all-atom empirical potentials: Fe in myoglobin. *J. Phys. Chem. B*. 109:18983–18987.
 88. Cusack, S., and W. Doster. 1990. Temperature dependence of the low frequency dynamics of myoglobin. Measurement of the vibrational frequency distribution by inelastic neutron scattering. *Biophys. J.* 58:243–251.
 89. Bauminger, E. R., S. G. Cohen, I. Nowik, S. Ofer, and J. Yariv. 1983. Dynamics of heme iron in crystals of metmyoglobin and deoxymyoglobin. *Proc. Natl. Acad. Sci. USA*. 80:736–740.
 90. Dilg, A. W. E., K. Grantner, O. Iakovleva, F. G. Parak, E. Babini, I. Bertini, F. Capozzi, C. Luchinat, and W. Meyer-Klaucke. 2002. Dynamics of wild-type HiPIPs: a Cys⁷⁷Ser mutant and a partially unfolded HiPIP. *J. Biol. Inorg. Chem.* 7:691–703.
 91. Markelz, A. G., J. R. Knab, J. Y. Chen, and Y. He. 2007. Protein dynamical transition in terahertz dielectric response. *Chem. Phys. Lett.* 442:413–417.

92. Wong, C. F., C. Zheng, and J. A. McCammon. 1989. Glass transition in SPC/E water and in a protein solution: a molecular dynamics simulation study. *Chem. Phys. Lett.* 154:151–154.
93. Loncharich, R. J., and B. R. Brooks. 1990. Temperature dependence of dynamics of hydrated myoglobin: comparison of force field calculations with neutron scattering data. *J. Mol. Biol.* 215:439–455.
94. Vitkup, D., D. Ringe, G. A. Petsko, and M. Karplus. 2000. Solvent mobility and the protein “glass” transition. *Nat. Struct. Biol.* 7:34–38.
95. Angell, A. 1998. Thermodynamics: liquid landscape. *Nature.* 393:521–524.
96. Adams, K., S. Tsoi, J. Yan, S. Durbin, A. Ramdas, W. Cramer, W. Sturhahn, E. Alp, and C. Schulz. 2006. Fe vibrational spectroscopy of myoglobin and cytochrome *f*. *J. Phys. Chem. B.* 110:530–536.
97. Takano, T., and R. E. Dickerson. 1981. Conformation change of cytochrome *c*: II. Ferrocycytochrome *c* refinement at 1.5 Å resolution. *J. Mol. Biol.* 153:95–115.
98. Takano, T., and R. E. Dickerson. 1981. Conformation change of cytochrome *c*: I. Ferricytochrome *c* refinement at 1.8 Å and comparison with the ferrocycytochrome structure. *J. Mol. Biol.* 153:79–94.
99. Sanishvili, R., K. Volz, E. Westbrook, and E. Margoliash. 1995. The low ionic strength crystal structure of horse cytochrome *c* at 2.1 Å resolution and comparison with its high ionic strength counterpart. *Structure.* 3:707–716.
100. Feng, Y., H. Roder, and S. W. Englander. 1990. Redox-dependent structure change and hyperfine nuclear magnetic resonance shifts in cytochrome *c*. *Biochemistry.* 29:3494–3504.
101. Gao, Y., J. Boyd, G. J. Pielak, and R. J. P. Williams. 1991. Comparison of reduced and oxidized yeast iso-1-cytochrome *c* using proton paramagnetic shifts. *Biochemistry.* 30:1928–1934.
102. Qi, P. X., R. A. Beckman, and A. J. Wand. 1996. Solution structure of horse heart ferricytochrome *c* and detection of redox-related structural changes by high-resolution ¹H NMR. *Biochemistry.* 35:12275–12286.
103. Trewthella, J., V. A. P. Carlson, E. H. Curtis, and D. B. Heidorn. 1988. Differences in the solution structures of oxidized and reduced cytochrome *c* measured by small-angle x-ray scattering. *Biochemistry.* 27:1121–1125.
104. Tiede, D. M., R. Zhang, and S. Seifert. 2002. Protein conformations explored by difference high-angle solution x-ray scattering: oxidation state and temperature dependent changes in cytochrome *c*. *Biochemistry.* 41:6605–6614.
105. Cusack, S., J. Smith, J. Finney, M. Karplus, and J. Trewthella. 1986. Low frequency dynamics of proteins studied by neutron time-of-flight spectroscopy. *Physica B (Amsterdam).* 136:256–259.
106. Sagle, L. B., J. Zimmermann, S. Matsuda, P. E. Dawson, and F. E. Romesberg. 2006. Redox-coupled dynamics and folding in cytochrome *c*. *J. Am. Chem. Soc.* 128:7909–7915.
107. Ward, N. L., O. Larsen, J. Sakwa, L. Bruseth, H. M. Khouri, A. S. Durkin, G. Dimitrov, L. Jiang, D. Scanlan, K. H. Kang, M. R. Lewis, K. E. Nelson, B. A. Methé, M. Wu, J. F. Heidelberg, I. T. Paulsen, D. E. Fouts, J. Ravel, H. Tettelin, Q. Ren, T. D. Read, R. T. DeBoy, R. Seshadri, S. L. Salzberg, H. B. Jensen, N. K. Birkeland, W. C. Nelson, R. J. Dodson, S. H. Grindhaug, I. E. Holt, I. Eidhammer, I. Jonassen, S. Vanaken, T. R. Utterback, T. V. Feldblyum, C. M. Fraser, J. R. Lillehaug, and J. Eisen. 2004. Genomic insights into methanotrophy: the complete genome sequence of *Methylococcus capsulatus* (Bath). *PLoS Biol.* 2:1616–1628.
108. Nakashima, T., H. Higa, H. Matsubara, A. M. Benson, and K. T. Yasunobu. 1966. The amino acid sequence of bovine heart cytochrome *c*. *J. Biol. Chem.* 241:1166–1177.
109. Landau, L. D., and E. M. Lifshitz. 1958. *Statistical Physics*. Pergamon Press, London.
110. Gerstein, M., J. Tsai, and M. Levitt. 1995. The volume of atoms on the protein surface: calculated from simulation, using Voronoi polyhedra. *J. Mol. Biol.* 249:955–966.
111. Tsai, J., R. Taylor, C. Chothia, and M. Gerstein. 1999. The packing density in proteins: standard radii and volumes. *J. Mol. Biol.* 190:253–266.
112. Lide, D. R. 2006. *CRC Handbook of Chemistry and Physics*, 87th Ed. CRC Press, Boca Raton, FL.
113. Kharakoz, D. P. 2000. Protein compressibility, dynamics, and pressure. *Biophys. J.* 79:511–525.
114. Eden, D., J. B. Matthew, J. J. Rosa, and F. M. Richards. 1982. Increase in apparent compressibility of cytochrome *c* upon oxidation. *Proc. Natl. Acad. Sci. USA.* 79:815–819.
115. Kharakoz, D. P., and A. G. Mkhitarian. 1986. Change in the compressibility of cytochrome *c* globule upon redox transition. *Mol. Biol. (Mosk.).* 20:396–401.